Nanostructured materials for lithium-ion batteries: Surface conductivity *vs.* bulk ion/electron transport

B. Ellis,[a] P. Subramanya Herle,[a] Y.-H. Rho,[a] L. F. Nazar,*[a] R. Dunlap,[b] Laura K. Perry[c] and D. H. Ryan[c]

Received 22nd February 2006, Accepted 9th May 2006
First published as an Advance Article on the web 7th August 2006
DOI: 10.1039/b602698b

Lithium metal phosphates are amongst the most promising cathode materials for high capacity lithium-ion batteries. Owing to their inherently low electronic conductivity, it is essential to optimize their properties to minimize defect concentration and crystallite size (down to the submicron level), control morphology, and to decorate the crystallite surfaces with conductive nanostructures that act as conduits to deliver electrons to the bulk lattice. Here, we discuss factors relating to doping and defects in olivine phosphates $LiMPO_4$ (M = Fe, Mn, Co, Ni) and describe methods by which *in situ* nanophase composites with conductivities ranging from 10^{-4}–10^{-2} S cm^{-1} can be prepared. These utilize surface reactivity to produce intergranular nitrides, phosphides, and/or phosphocarbides at temperatures as low as 600 °C that maximize the accessibility of the bulk for Li de/insertion. Surface modification can only address the transport problem in part, however. A key issue in these materials is also to unravel the factors governing ion and electron transport within the lattice. Lithium de/insertion in the phosphates is accompanied by two-phase transitions owing to poor solubility of the single phase compositions, where low mobility of the phase boundary limits the rate characteristics. Here we discuss concerted mobility of the charge carriers. Using Mössbauer spectroscopy to pinpoint the temperature at which the solid solution forms, we directly probe small polaron hopping in the solid solution Li_xFePO_4 phases formed at elevated temperature, and give evidence for a strong correlation between electron and lithium delocalization events that suggests they are coupled.

Introduction

The creation of redox-active transition metal framework structures that host mobile interstitial Li^+ ions is crucial in developing high capacity lithium-ion batteries. Lithium transition metal phosphates such as $LiFePO_4$,[1] $LiMnPO_4$,[2] $Li_3V_2(PO_4)_3$[3] and $LiVPO_4F$[4] have been recognized as promising positive electrodes for these systems because of their energy storage capacity combined with electrochemical and thermal stability. These are related either to fast-ion conducting phases, or minerals

[a] *University of Waterloo, Department of Chemistry, Waterloo, Ontario Canada N2L 3G1*
[b] *Department of Physics, Dalhousie University, Halifax, Canada*
[c] *Department of Physics, McGill University, Montreal, Canada*

such as olivine and tavorite. Owing to the inherently low electronic conductivity in the bulk it is absolutely essential to optimize their properties to obtain good electrochemical characteristics. This includes modification of crystal growth to minimize lattice defects and particle size (hence reducing the path length for electron and lithium ion transport), and modification of the crystallite surface to create conductive species that can act as "electronic wires" to feed electrons into the lattice without blocking access of lithium. Critical factors include how to design and tailor the ideal nanostructure and determine what its optimum morphology would be, and the nature of the interface.

A group of materials that serve as a good model for developing these concepts are the $LiMPO_4$ phosphates (M = Fe, Co, Ni, Mn), the most prominent members of a family of the polyanion compounds.[1,5] Their promise is due to the "inductive effect" of the XO_4 (X = Si, S, P) polyanion, which elevates the M^{2+}/M^{3+} redox couple by about 1.5–2 V for X = P.[6] A redox potential of 3.45 V *vs.* Li/Li^+ results in the case of $LiFePO_4$, making it a particularly appealing material for hybrid energy systems where cost and safety are of major concern. Both the Fe and Mn compositions are also attractive owing to their low environmental impact. The $Mn^{2+}/^{3+}$ couple is raised to a very desirable potential of 4.1 V in the phosphate framework; however, extraction of Li from this material is both slow, and incomplete due to a combination of factors that are not fully understood. These pertain to the Jahn–Teller distortion experienced by Mn^{3+} which creates mechanical stress in the lattice at high levels of oxidation.[7,8] Efforts to overcome this drawback have been successful to varying degrees.[9] Consideration of the inductive effect and preliminary electrochemical studies show both $LiCoPO_4$ and $LiNiPO_4$ will have very high redox couples (4.8 and >5.0 V, respectively), making them suitable only in the presence of an electrolyte with very high oxidation stability.[10]

The $LiMPO_4$ family adopts a common structure displayed by silicate minerals such as olivine, $MgFeSiO_4$, that constitute a large fraction of the earth's crust. The lattice comprises a network of MO_6^{n+} octahedra interwoven with XO_4^{n-} tetahedra. The mobile alkali ions, Li^+ in the case of $LiMPO_4$, form one-dimensional chains in the structure that run parallel to planes of corner-shared MO_6 octahedra, and along the [010] direction. Calculations of "free" ion transport in the absence of interactions with localized electron sites in the lattice suggest that the ion mobility along the chain direction is high,[11] but the material does not appear to be a fast ion conductor.[12] The electronically insulating effect of the tetrahedral XO_4^{n-} groups on which the inductive effect relies gives rise to isolation of the redox centers within the lattice. Correspondingly, incorporation of a XO_4^{n-} polyanion, such as phosphate, increases the band gap *vis a vis* the oxide to values that are in the range of 3.7 eV in $LiFePO_4$ based on both calculations and experiment.[13] Electron transport in this very poor semiconductor ($\sigma \approx 10^{-9}$ S cm^{-1}) is dependent upon small polaron hopping of Fe^{3+} holes within the lattice. Recent calculations predict an activation energy of 0.185 eV for a "free polaron" carrier in the absence of ionic interactions.[14]

The consequence of electronic transport limitation has led to immense efforts to overcome it, including methods to coat the phosphate particles with carbon,[15] embed them in a carbon matrix,[16] and lay down metal particles to form a composite.[17] The latter have all resulted in an increase in the working capacity of the material to approach theoretical capacity at relatively fast rates of electron extraction and insertion in the material. Another recently explored avenue is doping the framework with a supervalent ion to render it inherently conductive. The proposition was made that doping induced formation of a mixed valent state at the iron centers of Fe^{2+}/Fe^{3+}. Doped compositions $Li_{0.99}M_{0.01}FePO_4$ (M = Nb, Zr, Mg, Ti) were reported to be black p-type semiconductors with conductivities as high as $\sim 10^{-2}$ S cm^{-1} at room temperature.[18] Hole conductivity was suggested to arise from the formation of minority type Fe^{3+} carriers within the lattice. Since the stoichiometry as presented in fact suggests a sub-valent $<2+$ state of Fe in the case of Nb, Zr and Ti doping, loss of lithium is necessary to account for such an effect. Interest in this report stemmed

not only from the good performance of the material as a Li-ion electrode, but also from the 8-fold order of magnitude increase in conductivity. The origin and reproducibility of the conductivity have since been the source of extensive controversy (and many studies on doping) with speculation arising because the results violate commonly held concepts of electron mobility in this class of materials.

Another property of metal phosphates is their propensity to undergo carbothermal reduction. The reaction with carbon and $LiFePO_4$ results in oxidation of the carbon to CO or CO_2, and reduction of the neighboring Fe and P ions in the lattice to form Fe_2P and/or Fe_3P. This well known reaction has been recently used to reduce Fe^{3+} to Fe^{2+} to form $LiFePO_4$ from Fe^{3+} precursors, where control of the oxygen partial pressure and temperature is necessary to inhibit iron phosphide formation.[19] Higher temperatures result in reduction to Fe_2P whose presence in the bulk at temperatures above 850 °C has been implicated.[20] Unequivocal evidence for Fe_2P formation has been observed by X-ray diffraction, when sufficiently large amounts of carbon are present.[21] Careful control of such a reaction can result in intergranular conductivity in nanophase composites, and as we have demonstrated in a preliminary communication,[22] is responsible for the enormous enhancement of conductivity observed in carbon-containing $LiFePO_4$. As we show here, the reaction is general and even more favoured in metal phosphates of higher oxidizing potential such as $LiCoPO_4$, and $LiNiPO_4$, but not $LiMnPO_4$, and is responsible for the previously reported enhanced conductivity in Cr-doped $LiFePO_4$.[23] The use of lower reduction temperatures in more reducing atmospheres allows the reaction to be sustained at temperatures that maximize the surface area and accessibility of the material for Li insertion reactions. Nitridation can also be accomplished through the use of reactive gases that produce Fe_2N, and results in an increase in conductivity.

Since such surface structures can only partially solve the transport problem, a key issue in these materials is to furthermore disentangle the factors governing ion and electron transport within the lattice. Important to this is the creation of solid solutions over a wide lithium concentration range to facilitate coupled ion and electron transport. Such solid solutions were shown to form in $Li_{3-x}V_2(PO_4)_3$, for example, by disorder of V^{4+}/V^{5+} ions in the oxidized lattice that drives the delocalization of lithium ions.[24] In the $LiMPO_4$ family of materials, extraction of lithium forms a two-phase $LiMPO_4/MPO_4$ mixture that is in part driven by volume change between the structures. However, it was recently demonstrated that a transition to a Li_xFePO_4 solid solution (SS) phase occurs at about or above 485 K, where lithium occupation is random within the lattice.[25] Here we show using Mössbauer spectroscopy that electron delocalization in the solid solution phases is due to rapid small polaron hopping. We also show that the onset temperature of *electron* delocalization is correlated to the state of lithium disorder, suggesting the two transport mechanisms are coupled. Thus, the transport is limited by neither carrier alone, but by their concerted mobility through the lattice. This provides insight into the transport mechanism not only in $LiFePO_4$, but in an ever increasing family of phosphate, fluorophosphate and silicate materials being considered as the new generation of lithium-ion cathodes.

Experimental

Synthesis

Several solid state methods have now been described in the literature for the formation of $LiFePO_4$, triphylite, including (a) reaction of precursors such as $FeC_2O_4 \cdot 2H_2O/NH_4H_2PO_4/Li_2CO_3$ followed by treatment in various gases; (b) reaction of iron(III) precursors such as $FePO_4$ with lithium sources followed by treatment in reducing gases; and (c) precipitation of vivianite $Fe_3(PO_4)_2 \cdot 8H_2O$ and reaction with Li_3PO_4 followed by treatment in inert gases. All three methods were used in this study. Oxalates of nickel, cobalt and manganese were used to synthesize

the corresponding phospho-olivines, according to procedure (a). A typical process for the synthesis of triphylite involves the rigorous ball milling of the solid precursors in stoichiometric amounts, followed by sintering at 350 °C for 6 h. Final sintering of the powder occurs at 600–700 °C under various atmospheres (Ar, 7% H_2 in N_2, NH_3) for 2–10 h. Further treatment involved the pressing of a circular pellet (12 mm diameter under 3 tons of pressure) and sintering in flowing Ar at 800–1000 °C for various compositions.

XRD, STEM and SEM

X-Ray diffraction was performed on a Bruker D8-Advantage powder diffractometer using Cu Kα radiation (λ = 1.5405 Å) from 2θ = 10–80° at a scan rate of 6 s per step of 0.01°. X-Ray data sets were refined by conventional Rietveld methods using the GSAS package with the EXPGUI interface.[26] The background, scale factor, zero point, lattice parameters, atomic positions, and coefficients for the peak shape function were iteratively refined until convergence was achieved. TEM analysis was carried out by embedding a small portion of the sintered pellet in epoxy resin, and slicing the sample with an ultramicrotome. The slice was supported on a 200 mesh Cu grid. STEM imaging and EDX spot elemental analysis was performed using a Hitachi S5200 operating at 30 kV in STEM mode to determine the Fe : P ratios. SEM samples were gold coated and examined in a LEO 1530 field emission scanning electron microscope (FESEM) instrument equipped with an energy dispersive X-ray spectroscopy (EDX) attachment. Images were recorded at 15 kV with a secondary electron detector.

X-Ray photoelectron spectroscopy

Materials were analyzed with a VG Scientific XPS Microprobe ESCA Lab 250 using focused monochromatic Al Kα radiation (1486.6 eV). Samples were deposited on a Cu substrate with an irradiated area of 0.4 × 1 mm^2, and loaded in the chamber at a pressure of less than 10^{-10} mbar.

Conductivity measurements

Pellet surfaces were polished prior to variable temperature conductivity measurements that were performed using four-point d.c. methods. Electrode contacts were affixed using silver or gold paste in linear geometry on a thin section of a pellet of approximate dimensions: 1 mm × 1 mm × 5 mm.

Electrochemical measurements

Electrochemical evaluation of the materials were carried out in coin cells using a commercial (MacPile™) multichannel galvanostat/potentiostat operating in galvanostatic mode. Typical cathode loadings were in the range of 5–6 mg cm^{-2} and an electrode diameter of 10 mm was used throughout. The positive electrodes comprised 80 wt% active material, 10% Super S carbon and 10 wt% PVdF binder. The electrolyte was composed of a 1 M $LiPF_6$ solution in 1 : 1 EC–DMC; and the anode consisted of lithium metal supported on a stainless steel disc.

Results and discussion

(a) Cation occupation, doping and substoichiometry

The olivine structure represented by $LiMPO_4$ (*i.e.*, $ABXO_4$, where X = Si, P, B, Be) contains two crystallographic sites occupied by the A and B cations, as seen in Fig. 1. Both sites (known as M1 and M2) can be described as having slightly distorted octahedral co-ordination. In iron–magnesium silicate olivines that form a solid

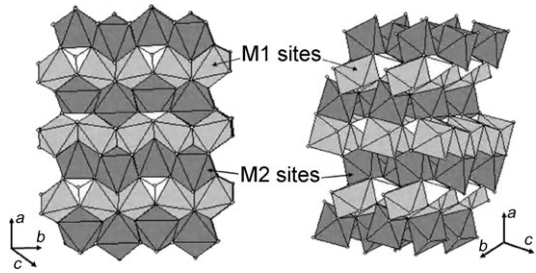

Fig. 1 The olivine structure, adopted by several minerals including $LiFePO_4$. The octahedral M1 (Li) and M2 (Fe) cation sites are labelled; the bridging phosphate groups are shown as tetrahedra.

solution composition between fayalite (Fe_2SiO_4) and forsterite (Mg_2SiO_4), there is disorder of the 2+ cations on the M1 and M2 sites. When the metal cations differ in charge however (such as the case of $LiFePO_4$), there is generally strict ordering of ions in these metal sites based on size and energy preferences: the M2 site houses the cation of greater charge. However, low temperature syntheses at 130 °C based on hydrothermal chemistry have been reported to yield disorder as high as 7%.[27]

A starting point for our investigations was to examine the consequence of Li substoichiometry and doping of cations on the M1 and M2 sites. The reason was two-fold: first, evidence from Fe-substituted nickel phosphates such as $Li_{1-3x}Fe_x$-$NiPO_4$ suggest that olivine phosphates can be synthesized with sustainable cation vacancies on the M1 site,[28] thus the direct synthesis of any lithium deficient iron phosphates that are able to sustain solid solution behaviour at room temperature would indeed be novel. Second, as mentioned above, compositions with very low dopant levels such as $Li_{0.99}M_{0.01}FePO_4$ (where M = Mg^{2+}, Al^{3+}, Zr^{4+}, Nb^{5+}) have been reported.[12] Since the nominal stoichiometries imply a sub-valent state of Fe ($<Fe^{2+}$) on the basis of charge balance (*i.e.*, for $Li_{0.99}Zr_{0.01}FePO_4$, the formal oxidation state of iron would be +1.97), loss of lithium during processing would have to occur to account for Fe^{3+} hole carrier formation. The dopant could act as a stabilizer. The precise site occupancy of these dopants was not established, however. These results have stimulated considerable debate about the precise defect properties. Cation doping of $LiFePO_4$ raises key questions as to the favored substitution site (M1 *versus* M2), the type of compensating defect, and whether the doping process is favorable on energetic grounds. Our preliminary work that examined the compositions $Li_xZr_{0.01}FePO_4$ (x = 0.87 to 0.99) showed that dopants were not essential, and suggested that percolating "nano-networks" of metal-rich phosphides within the grain boundaries of $LiFePO_4$ crystallites are responsible for the enhanced electronic conductivity.[22] Recent structural and electrochemical studies of Delacourt *et al.* were also unsuccessful in Nb doping of $LiFePO_4$; instead, they showed that crystalline α-$NbOPO_4$ and/or an amorphous (Nb, Fe, C, O, P) coating was formed around $LiFePO_4$ particles, which is believed to be responsible for the superior electrochemical activity.[29] In accord with these experimental results are recent calculations reported by Islam *et al.*, that examined a range of dopants including divalent (*e.g.*, Mg, Mn, Co), trivalent (*e.g.*, Al, Ga, Y), tetravalent (*e.g.*, Zr, Ti), and pentavalent (*e.g.*, Nb, Ta) ions.[30] Their calculations reveal that low favorable energies are found only for divalent dopants on the Fe (M2) site (such as Mg and Mn). On energetic grounds, $LiFePO_4$ is not tolerant to aliovalent doping (*e.g.*, Al, Ga, Zr, Ti, Nb, Ta) on either Li (M1) or Fe (M2) sites.

Our attempts to dope the $LiFePO_4$ lattice are consistent with these findings. We chose Zr^{4+} as a target dopant since the calculated effective ionic radii of Li^+ and Zr^{4+} (0.76 and 0.72, respectively) are sufficiently similar that Zr could easily substitute onto a lithium site. Table 1 summarizes refined lattice parameters for various stoichiometries, synthesized with iron oxalate, with both lithium and iron or

Table 1 Refined lattice parameters of olivine phases after addition of supervalent cations to probe the presence of doping and possible site preferences for the dopant

Dopant target site(s)	Stoichiometry	Refined olivine lattice parameters			Detectable impurities
		a/Å	b/Å	c/Å	
None	$LiFePO_4$	10.3203(2)	6.0045(1)	4.6934(2)	None
M1	$Li_{0.96}Zr_{0.01}FePO_4$	10.3203(3)	6.0041(2)	4.6957(3)	Below detection limit
M1	$Li_{0.88}Zr_{0.03}FePO_4$	10.3260(2)	6.0047(1)	4.6948(1)	NASICON-structured phosphate
M1	$Li_{0.99}Zr_{0.01}FePO_4$	10.3221(3)	6.0049(1)	4.6924(2)	None
M1	$Li_{0.91}Cr_{0.03}FePO_4$	10.3262(2)	6.0050(1)	4.6935(1)	Cr_2O_3, $Fe_2P_2O_7$
M1/M2	$Li_{0.94}Al_{0.06}Fe_{0.94}PO_4$	10.3210(2)	6.0052(2)	4.6941(1)	$AlPO_4$
M1/M2	$Li_{0.94}Y_{0.06}Fe_{0.94}PO_4$	10.3183(3)	6.0040(1)	4.6925(1)	YPO_4

simply lithium deficiencies. The data for the former does not indicate that doping of the olivine structure has taken place, owing to the minimal changes in the lattice parameter for pristine triphylite and the considerable presence of impurity phases produced which account for the preponderance of the supervalent cation population. To determine the extent of Zr doping in the lattice, $Li_{1-4x}Zr_xFePO_4$ compositions ($0 < x < 0.05$) were heated to 600 °C under an inert atmosphere in microcrystalline form. Fig. 2 shows X-ray diffraction patterns of the materials. The composition $Li_{0.96}Zr_{0.01}FePO_4$ fits well with the database pattern for $LiFePO_4$, suggesting that a small degree of lithium non-stoichiometry may be sustained within the lattice, as suggested by a very recent report.[31] However the XRD pattern for $Li_{0.88}Zr_{0.03}FePO_4$ clearly shows the presence of a new phase that is likely a mixed Li–Zr–Fe phosphate with a NASICON structure, as the lines index well to those of $LiZr_2(PO_4)_3$.[32] Determination of the lattice parameters of the olivine phase by Rietveld analysis did not clearly indicate that Zr substitution on the M1 site in the olivine occurred, as outlined in Table 1. It is expected, based on previous studies of Fe substituted $LiNiPO_4$ phases ($Li_{1-3x}Fe_xNiPO_4$), that the a and b lattice parameters would experience a small decrease with Zr substitution owing to the presence of vacancies on M1, and that c would undergo a slight increase.[28] This is observed for $Li_{0.96}Zr_{0.01}FePO_4$, but the change (±0.15%) is barely significant. In the case of $Li_{0.88}Zr_{0.03}FePO_4$, the change in lattice parameter is minute and opposite to that

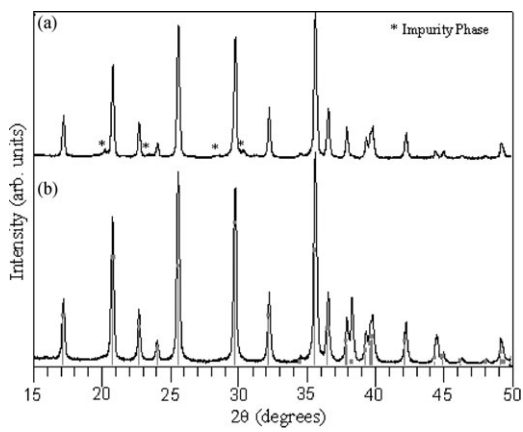

Fig. 2 X-Ray diffractograms of Zr doped materials (a) $Li_{0.88}Zr_{0.03}FePO_4$ and (b) $Li_{0.96}Zr_{0.01}$-$FePO_4$ prepared at 600 °C. A NASICON-structured impurity phase becomes evident at high lithium non-stoichiometry, indicated by the asterisks in the diffraction pattern of (a).

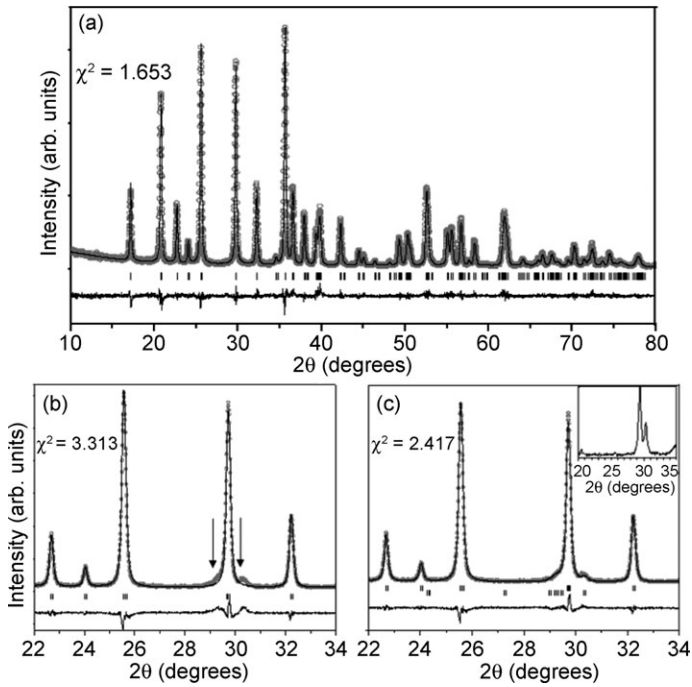

Fig. 3 Experimental X-ray (○) and calculated diffraction patterns (-) based on Rietveld refinement together with the (*hkl*) reflections (|) and the difference curve of: (a) pristine olivine $LiFePO_4$ (refined cell: a = 10.3172(4) Å; b = 6.0018(2) Å; c = 4.6906(1) Å); (b) a representative sample of a lithium-deficient material, $Li_{0.91}FePO_4$ refined with only $LiFePO_4$, showing the contribution of iron pyrophosphate (arrows); (c) refinement using a two-phase mixture of $LiFePO_4$ and $Fe_2P_2O_7$ (lower phase tags in (c); refined cell: a = 5.5032(2) Å; b = 5.2759(2) Å; c = 4.4760(2) Å; α = 98.353(3)°; β = 98.539(3)°; γ = 104.009(4)°), indicating the significant improvement in the refinement. The XRD pattern of $Fe_2P_2O_7$ alone is shown in the inset in (c). The phase mixture fraction of all materials based on Rietveld analysis are listed in Table 2.

expected for a and b. Hence we conclude that if doping is sustainable, it is only at very low levels (*i.e.*, <3%).

We endeavoured to determine whether lithium deficient triphylite materials could be synthesized directly and uncover the possible stabilizing effects of very low amounts of Zr-doping. Following the original procedure, $Li_xZr_{0.01}FePO_4$ powdered materials ($0.99 < x < 0.87$) were heated to 600 °C under inert atmosphere. Lithium deficient samples of Li_yFePO_4 ($0.88 < y < 1$) were also prepared without the addition of the zirconium isopropoxide dopant, chosen to be "valent-equivalent" to the Zr-doped samples. The resultant XRD patterns for representative crystalline powders are shown in Fig. 3. The materials prepared are almost entirely pure: compositions that are close to stoichiometric (such as $Li_{0.97}FePO_4$ or $Li_{0.96}Zr_{0.01}FePO_4$) show only reflections due to single-phase $LiFePO_4$ (Fig. 3a). Closer inspection reveals that as the Li content decreases, a slight broadening in the (020) reflection at 29.7 and 30.3° in 2θ becomes evident, which can ultimately be resolved as very weak satellite lines attributable to $Fe_2P_2O_7$, the diffraction pattern of which is shown in Fig. 3c (inset). The agreement factors in the Rietveld fit increase markedly with the addition of this impurity phase to the refinement, as seen for $Li_{0.91}FePO_4$ (Fig. 3b and c). The weight and molar percentage of each phase present are summarized in Table 2. The calculated quantity of lithium in each sample closely matches the original pyrophosphate impurity, which increases linearly with lithium substoichiometry for both the Zr-containing and undoped compositions. Thus, it is

Table 2 Composition of two-phase mixtures formed from heat treatment of Li-deficient stoichiometries heat treated at 600 °C

Compound	$LiFePO_4$/mol%	$Fe_2P_2O_7$/mol%
$LiFePO_4$	100.0	—
$Li_{0.97}FePO_4$	98.1	1.9
$Li_{0.94}FePO_4$	95.7	4.3
$Li_{0.91}FePO_4$	91.8	8.2
$Li_{0.88}FePO_4$	88.8	11.2
$Li_{0.99}Zr_{0.01}FePO_4$	99.5	—
$Li_{0.96}Zr_{0.01}FePO_4$	97.5	2.5
$Li_{0.93}Zr_{0.01}FePO_4$	92.1	7.9
$Li_{0.90}Zr_{0.01}FePO_4$	89.1	10.9

conceivable that a metastable substoichiometric $Li_{(1-x)}FePO_4$ phase initially forms, with a stability regime between ~200–400 °C as recently reported.[18] This phase then decomposes to $(1-x)$ $LiFePO_4$ + $x/2$ $Fe_2P_2O_7$ at temperatures above 600 °C. In turn, the pyrophosphate undergoes carbothermal reduction to iron phosphide at 800 °C, a lower temperature than that for $LiFePO_4$.

Further proof that substoichiometric Li compositions decompose to $Fe_2P_2O_7$ and fail to form Fe^{3+} hole carriers as a method of charge compensation was attained from direct analysis of the Fe^{3+} content by Mössbauer spectroscopy. The spectrum of a highly conductive $Li_{0.90}Zr_{0.01}FePO_4$ sample pellet is shown in Fig. 4. The fitted parameters are: isomer shift (IS) 1.217 mm s^{-1}; quadrupole splitting (QS) 2.905 mm s^{-1} and width 0.19 mm s^{-1} which are typical of octahedrally coordinated Fe^{2+} in $LiFePO_4$. The impurity phase $Fe_2P_2O_7$ is not visible in the Mössbauer spectrum. As iron is in the same oxidation state and similar coordination in this material, its Mössbauer parameters are similar to those for $LiFePO_4$ and this component lies under the signal for the majority phase $LiFePO_4$. The spectrum for a Fe^{+3} ion in octahedral coordination features a symmetric doublet; the quadrupole splitting for orthorhombic $FePO_4$ is 1.53 mm s^{-1}.[2] A least-squares fit to the spectrum that

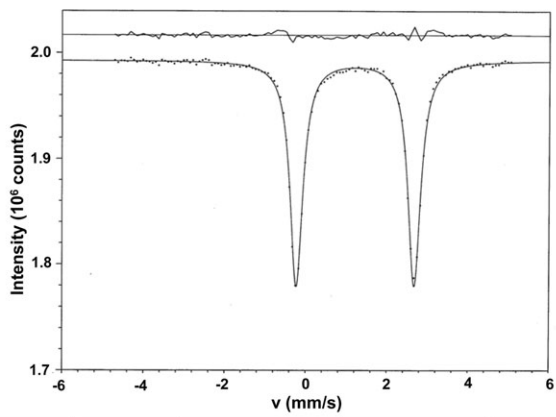

Component	Center shift (mm/s)	Quadrupole splitting (mm/s)	Linewidth (HWHM) (mm/s)	Site population (%)
2+	1.217	2.905	0.19	97.9
3+	0.44 (fixed)	0.76	0.29	2.1

Fig. 4 Mössbauer spectrum of a highly conductive sample $Li_{0.90}Zr_{0.01}FePO_4$ sintered at 800 °C. The fitted parameters are typical of Fe^{2+} in $LiFePO_4$. The other minor Fe^{2+} contributor, $Fe_2P_2O_7$, that is visible in the XRD pattern lies under this Fe^{2+} component.

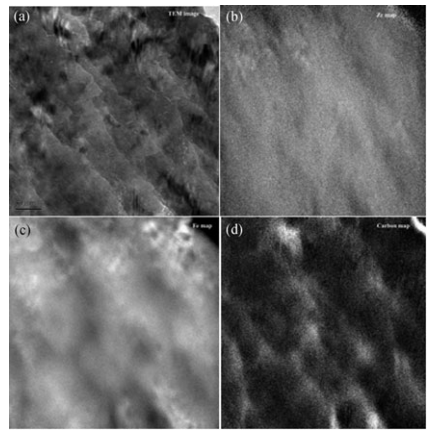

Fig. 5 TEM image of $L_{i0.90}Zr_{0.01}FePO_4$ pellet sintered at 800 °C showing (a) image; (b) Zr map; (c) Fe map, (d) C map.

included a second contribution from Fe^{3+} (with a "typical" fixed isomer shift of 0.44 mm s^{-1}) failed to yield any statistically significant evidence for its presence. At most, the Fe^{3+} contribution was 2%, and the quadrupole splitting did not match that of $FePO_4$. Thus, even with a 10% deficiency in Li content from pure $LiFePO_4$, the additional conductivity found in these composites cannot be predominately due to Fe^{+3} hole conductivity.

The total of the above observations strongly suggests that (a) Zr does not act as an internal dopant to stabilize lithium substoichiometry to any large extent; and (b) the Zr is likely primarily located on the surface of the particles. The latter is not surprising as the dopants were added as an alkoxide [*i.e.*, $Zr(OC_3H_7)_4 \cdot C_3H_7OH$], and the precursors were subjected to extensive ball-milling. This step effectively disperses the Zr (and more importantly, carbon from the alkoxide) but minimal Zr is incorporated into the olivine lattice. Indeed, EDX mapping of crystallites (Fig. 5) shows a uniform distribution of Zr both on the surface and within the grain boundaries of the crystallites. Finally, in the context of using dopants to increase electrochemical performance, it is worth noting that aliovalent doping of the M1 site (*i.e.* Mg^{2+}, Zr^{4+}, *etc.*) *could* potentially induce lithium vacancy formation, *i.e.*, $Li_{1-2x}Mg_xFePO_4$ at low levels. However transport of the Li^+ ions would be inhibited by the immobility of the dopant within the one-dimensional tunnels.

(b) Carbothermal reduction

Fig. 6 shows SEM images of the $LiFePO_4$ crystallites obtained after milling carbonaceous and non-carbonaceous precursors at 600 °C under flowing argon. The particle morphology of the former consists of aggregrates of primary nanoparticles <300 nm in dimension. This suggests, not surprisingly, that the carbon (whether from the iron oxalate, dopant alkoxide or both) binds strongly to the surface of the precursors, thus simultaneously coating the particle with carbon containing reagent, and restricting growth of the particles. Without the alkoxide carbon contribution, materials produced from vivianite yield a block-like morphology in large crystallite form.

Furthermore, the presence of carbon, either from the additional alkoxide or from the oxalate in the solid state route, is significant to the properties of the materials owing to the importance of carbothermal chemistry that occurs at high temperatures in these phosphates. Carbothermal reduction (CTR) is used extensively in industry to reduce metal oxides, such as ZnO, FeO, Cr_2O_3 and Al_2O_3 to pure metals.[33] Using

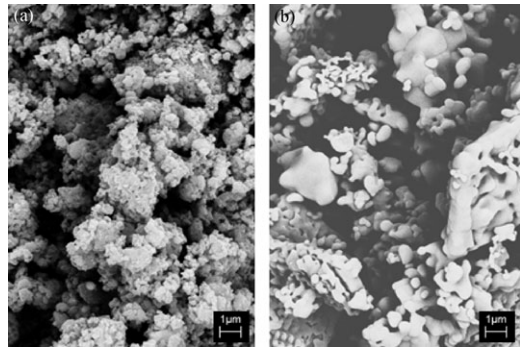

Fig. 6 SEM image of polycrystalline $LiFePO_4$ powders sintered at 600 °C prepared from (a) iron oxalate and (b) vivianite. Carbon present in the former controls particle size and morphology; particles average 300 nm in diameter.

the system of binary oxides as an example, the ease of reduction of a particular binary metal oxide can be described by the standard free energy of formation of the oxide, which is a measure of the affinity of the metal to be in an oxide lattice. The reduction can take place *via* two different carbon oxidation reactions:

$$C + O_2 \leftrightarrow CO_2 \quad (1)$$

$$2C + O_2 \leftrightarrow 2CO \quad (2)$$

The formation of carbon dioxide in eqn (1) represents a minimal volume change, and thus a change in entropy of almost zero. As a result, the standard free energy of formation of CO_2 is almost unchanged (-390 kJ mol^{-1}) regardless of temperature. However, the formation of carbon monoxide in eqn (2) involves an increase in entropy through an increase in volume of the system. Therefore, the standard free energy of formation of CO becomes increasingly negative as temperature increases. At approximately 700 °C, the formation of CO becomes more favourable than the formation of CO_2, resulting in stronger reducing conditions at higher temperatures. Slower kinetics and less reductive conditions exist at lower temperatures. As a result, it is theoretically possible to reduce any oxygen-containing mineral with carbon assuming a critical temperature is reached. A typical method of showing this information is an Ellingham plot of the standard free energy of compound formation *vs.* temperature for various metal oxide pairs; Table 3 summarizes the data of the Ellingham plot for oxide formation. The enthalpy of reduction increases with stability of the oxide so that very high temperatures are required (>1400 °C) to reduce very stable oxides such as MnO or MgO.

CTR has been previously reported as a solid state synthetic method for making lithium-containing battery materials, including $LiFePO_4$.[19] In that process, an excess of carbon is added to Fe_2O_3 and LiH_2PO_4 and the mixture is heated to 750 °C under argon. This reaction allows selective reduction (of only Fe^{+3}), simultaneous lithium incorporation into the lattice and provides a small excess of carbon at the conclusion

Table 3 Thermodynamic data for carbothermal reduction of selected binary oxides

Compounds	$-\Delta G^\circ$ at 600 °C/kJ mol O_2^{-1}	Minimum Temperature for CTR/°C
Mg/MgO	1040	1850
Mn/MnO	645	1420
Fe/FeO	420	710
Co/CoO	340	240
Ni/NiO	335	280

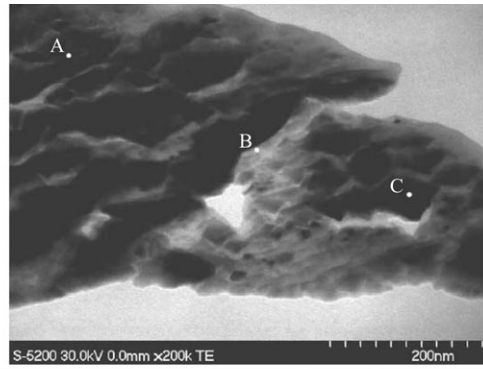

Region of Micrograph	Fe (atom%)	P (atom%)
Region A, bulk	49.4	50.6
Region B, grain boundary	62.3	37.7
Region C, bulk	53.3	46.7

Fig. 7 STEM image of sintered $Li_{0.90}Zr_{0.01}FePO_4$ collected using a Hitachi S5200 STEM operating at 30 kV EDX. EDX spot elemental analysis was used to determine the Fe : P ratios at the grain boundary and in the bulk, confirming the presence of iron phosphides at the grain boundaries.

of the reaction which is beneficial to electrode preparation. However, the carbothermal reduction of the olivines themselves has not been vigorously studied. Many synthetic methods of $LiFePO_4$ contain carbon, whether from decomposition of oxalates or acetates, or simply from the incorporation of additional carbon into the synthesis. These $LiFePO_4$–C composites are usually heated to temperatures near or above the minimum temperature for reducing iron oxide. Using the CTR data for oxides as a guide, it is clear that these conditions should result in reduction of the olivine phosphates to produce metal phosphide compounds (such as FeP, Fe_2P, Fe_3P in the case of $LiFePO_4$), many of which are metallic or semiconducting. If these compounds are produced in small quantities, they provide a conductive solid network to improve the overall conductivity of the olivine compounds, which was previously only possible by the addition of carbon (which decreases tap density).[34]

We have previously implicated the role of CTR in the increase in conductivity of $LiMPO_4$ (M = Fe, Ni) compounds. This enhancement is due to formation of a ''nano-network'' of electronically conductive species which forms at high temperatures, imaged by TEM and EELS mapping to reveal the presence of Fe_2P and carbon in the grain boundaries of the solid.[22] The onset of the enhanced conductivity commences near 800 °C for lithium-substoichiometric compounds, where we have observed the reduction of the $Fe_2P_2O_7$ present in these materials. Additional evidence for phosphides is shown in the STEM image (Fig. 7) of granules of $Li_{0.90}Zr_{0.01}FePO_4$. EDX analysis shows that the bulk of the crystallite (regions A, C) yields an iron to phosphorus ratio of roughly 1 : 1 as expected. However, the edge of the crystallite (region B) is significantly iron-rich with an Fe to P ratio of 2 : 1, indicating the presence of conductive Fe_2P. In combination with the carbon in the grain boundaries, this creates the nano-network which percolates through the entire sample. It is also likely that the amorphous metallic glass phase $Fe_{75}P_{20}C_{15}$ is formed at these temperatures by reaction of iron phosphide with carbon, which may serve to wet the grain boundary.

As departure from the original $LiFePO_4$ stoichiometry increases (and so does the $Fe_2P_7O_7$ content), the conductivity of the densified pellets increases. A summary of the conductivities of various starting stoichiometries is shown in Table 4. This value reaches a maximum near $x(Li) = 0.90$, after which the pellets are less dense, have a

Table 4 Room temperature conductivity values of lithium deficient $LiFePO_4$ composite pellets sintered at 800 °C

Stoichiometry	Conductivity @ 20 °C/S cm^{-1}
$LiFePO_4$	$<10^{-7}$
$Li_{0.97}FePO_4$	2.0×10^{-3}
$Li_{0.94}FePO_4$	6.5×10^{-3}
$Li_{0.91}FePO_4$	1.1×10^{-2}
$Li_{0.88}FePO_4$	$<10^{-7}$
$Li_{0.99}Zr_{0.01}FePO_4$	$<10^{-7}$
$Li_{0.93}Zr_{0.01}FePO_4$	5.1×10^{-4}
$Li_{0.90}Zr_{0.01}FePO_4$	5.3×10^{-3}
$Li_{0.87}Zr_{0.01}FePO_4$	$<10^{-7}$

more brittle texture and are no longer a deep black colour throughout. It is likely that the CTR reaction with $Fe_2P_2O_7$ has gone to completion, consuming the entire quantity of carbon in the grain boundaries, and leaving behind amorphous $Fe_x(P,C)_y$ without the connecting carbon infrastructure. The conductive nano-network is thus dismantled. In addition, dense pellets of carbon-free Li_xFePO_4 were prepared from vivianite ($x = 0.91, 0.94, 1.00$). These samples were each light grey and non-conductive ($\sigma < 10^{-7}$ S cm^{-1}), in contrast to $LiFePO_4$ prepared from iron oxalate at the same temperature, further demonstrating the role of carbon in the enhancement of conductivity in these materials.

Although electron transport in $LiFePO_4$ is a factor in poor electrochemical performance, the increase in conductivity *via* high temperature CTR does not benefit the electrochemistry of these materials. Fig. 8 shows the electrochemistry and conductivity plot of a conductive pellet of pristine $LiFePO_4$ sintered at 850 °C. Compared to $LiFePO_4$ powder sintered at 600 °C, the sample heated to higher

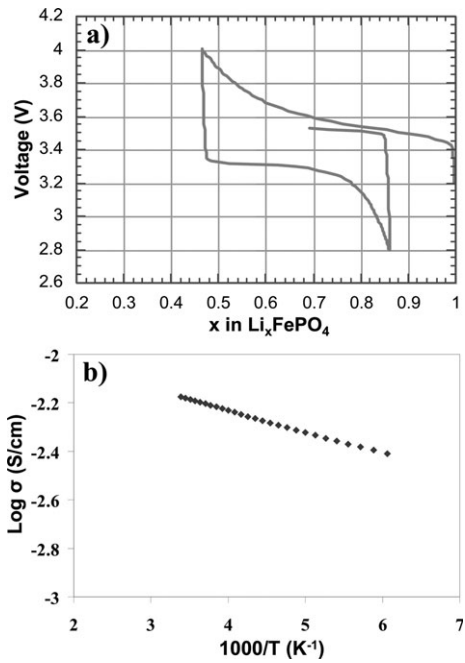

Fig. 8 (a) Electrochemistry and (b) electronic conductivity of a pelletized sample of $LiFePO_4$ sintered at 850 °C.

temperature has poor reversibility and a high polarization as a result of having a much larger particle size as a consequence of high temperature sintering.

(c) Carbothermal reduction of $LiMPO_4$ (M = Ni, Co, and Mn)

The concept of carbothermal reduction in $LiFePO_4$ was extended to other lithium metal phosphates including $LiNiPO_4$, which has a higher oxidation potential than $LiFePO_4$. Samples of Li_xNiPO_4 (x = 0.91–1.00) were prepared similarly to the corresponding iron compounds with the exception of atmosphere. Since $LiNiPO_4$ is stable at high temperatures under air and oxygen, it can be synthesized in oxidizing conditions which would promote formation of a mixed valent $Ni^{+2/+3}$ state for the lithium deficient stoichiometries while removing the possibility of phosphide formation. These oxidizing conditions can not be used to synthesize the iron compound, as $LiFePO_4$ oxidizes to $Li_3Fe_2(PO_4)_3$ in air above 400 °C.

Fig. 9 depicts X-ray diffraction patterns of powders and sintered pellets of $Li_{1-x}NiPO_4$ compositions prepared from carbon containing precursors. Single phase $LiNiPO_4$ is formed at 600 °C in air in both stoichiometric and slightly Li-substoichiometric compositions, resulting in bright yellow solids for all compositions. All showed no measurable gain in conductivity, showing values $<10^{-7}$ S cm^{-1}. Conversely, sintering of the carbon-containing nickel phosphate under inert gas at 600 °C yielded black powders. $LiNiPO_4$ is formed, along with other phosphate impurities such as $Li_4P_2O_7$, and $Li_2Ni_3(P_2O_7)_2$, as well as substantial quantities of Ni_3P, indicating that extensive carbothermal reduction of the phosphate has commenced prior to reaching this temperature. As a result, a pressed pellet sintered at 650 °C showed a significant (10^6) gain in conductivity (Fig. 10). The overall value is lower than for $LiFePO_4$ in part because the pellets are less densified at a lower temperature, and also because of the different nature and quantities of the phosphides within the grain boundary. Heat treatment of $LiNiPO_4$ composite pellets at temperatures above 650 °C produced pellets that are expanded and have a foamed texture (similar to that of pumice rocks), indicative of gas formation inside the solid. Clearly vigorous reduction resulting in the consumption of carbon and the subsequent release of CO and CO_2 takes place at these higher temperatures. A similar reaction also occurs in the case of $LiFePO_4$ made from iron oxalate; pellets sintered at temperatures >925 °C also expand and trap gas inside. These samples, however, are grey instead of black and are non-conductive, even though Fe_2P can be seen in the XRD pattern. This is a result of the phosphide crystallizing out of the grain

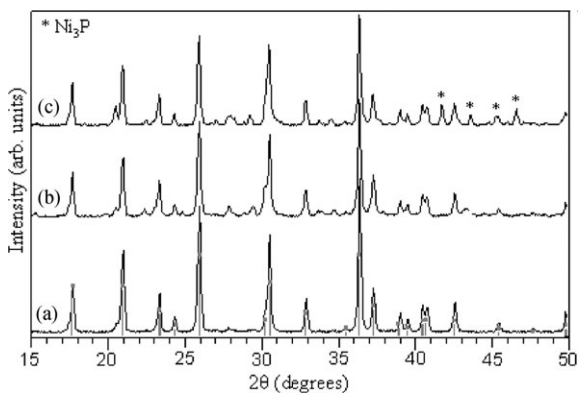

Fig. 9 Effect of sintering atmosphere on $LiNiPO_4$ composites: (a) $LiNiPO_4$ (600 °C, air); (b) $Li_{0.94}NiPO_4$ (600 °C, air); (c) $Li_{0.94}NiPO_4$ (600 °C, Ar) indicating the presence of substantial secondary phases including Ni_3P.

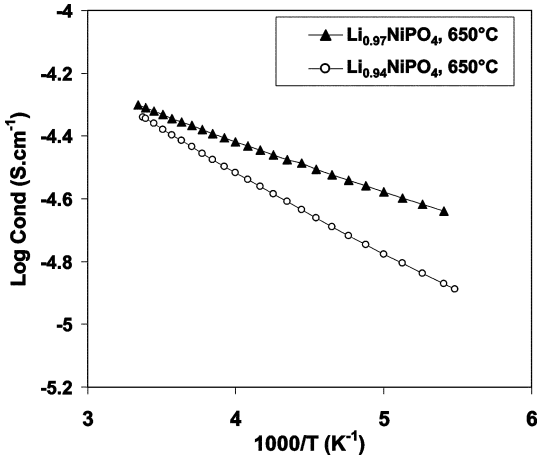

Fig. 10 Electronic conductivity plots of lithium-deficient Ni compounds in the presence of Ni_3P.

boundaries to form large particles, which, when combined with the consumption of carbon during this process, disconnects the conductive nano-network. We note that the temperature window between when iron phosphide/phosphocarbide begins to first form ($\sim$800 °C) and when it is extruded from the grain boundary as a result of Fe_2P crystallite growth (*i.e.*, 925 °C), is much broader than in the case of $LiNiPO_4$. Any iron phosphocarbide that is also formed (see above) may contribute to this wider stability range.

The mechanism for phosphide formation in the nickel compound differs from that for $LiFePO_4$. XRD patterns of the carbon-containing $LiNiPO_4$ precursors after the initial heat treatment at 350 °C show low intensity, poorly crystalline peaks which correspond to $LiNiPO_4$ and Li_3PO_4, and two high intensity peaks of metallic Ni. Thus the carbon from the nickel oxalate precursor reduces a portion of the metal to the elemental state. As the temperature of the reaction is increased to 600 °C, $LiNiPO_4$ crystallizes, along with Ni_3P and the other phosphate impurities. The peaks corresponding to nickel decrease and become very minor at this stage. We conclude that nickel metal is directly consumed in the production of Ni_3P or, due to the catalytic properties and reactivity of nickel nanoparticles, it is viable that it acts also as a catalyst, aiding the formation of Ni_3P by catalyzing the carbothermal reduction of $LiNiPO_4$.

In contrast, the remainder of the transition metal series of $LiMPO_4$ compounds (M = Mn, Fe, Co) do not undergo this early carbothermal reduction step. Each phosphate in this series is partially crystalline after firing at 350 °C under an inert atmosphere in the presence of trace amounts of carbon from the respective metal oxalate precursors. XRD reveals no traces of the respective metals. As a result, pure $LiMPO_4$ powders at 600 °C are produced; it is heat treatment at elevated temperatures that initiates the carbothermal reduction. In the case of $LiCoPO_4$, this process commences below 700 °C, as Co_2P and $Li_4P_2O_7$ are clearly seen in XRD patterns for powders fired at 700 °C. As stated previously for $LiFePO_4$, iron phosphide (and potentially) phosphocarbide formation occurs due to reduction at the grain boundaries at temperatures over 800 °C.

In the case of $LiMnPO_4$, the temperature for reduction is much higher than that for the other compounds, owing to the high thermodynamic stability of oxygen-containing Mn(II) compounds. We were unable to obtain any indications of reduction of carbon-containing $LiMnPO_4$ made from manganese oxalate at temperatures up to 1000 °C. Further attempts for reduction of $LiMnPO_4$, including the addition of 10 wt% carbon and firing in reducing atmospheres (in both NH_3 and a

mixture of 7% H_2 in N_2) at 1000 °C, also failed to show any trace of reduced species after sintering. These results are consistent with the high stability of MnO, which will only undergo CTR at temperatures in excess of 1400 °C based on the Ellingham curves. In theory, phosphide and phosphocarbide formation as a result of CTR can occur in any of the carbon-coated $LiMPO_4$ compounds; the carbon, which deposits in the grain boundaries between the crystallites, can initiate reduction once the onset temperature is reached.

(d) Synthesis in highly reducing atmospheres

Although the generation of phosphides and phosphocarbides has been shown to benefit electrical conductivity of bulk materials, the temperatures required to generate these species result in excessive particle growth and, as a result, are detrimental to electrochemical performance. However, it is well known that reduction of iron(III) precursors to $LiFePO_4$ using hydrogen gas as a reducing agent can be carried out at lower temperatures compared to some CTR reactions. This synthesis method has been used in various recent synthetic routes,[35] and was used in the attempted doping of $LiFePO_4$ with chromium. Band structure calculations suggested that the Fermi energy of the latter is at the edge of the Fe valence band and high electronic conductivity was measured in the Cr-doped materials.[23]

A sample of $Li_{0.91}Cr_{0.03}FePO_4$ was prepared exactly according to the cited literature method.[26] Contrary to the report, the powder, upon sintering at 700 °C for ten hours under a 7% H_2–N_2 atmosphere, reduced to a large fraction of Fe_2P and Li_3PO_4. As a result, the starting powder was re-fired at 700 °C under argon gas to limit the severity of the reducing conditions. The powder XRD pattern is shown in Fig. 11. As is the case with all lithium-deficient compounds, $Fe_2P_2O_7$ is prominent in the diffractogram. Also clearly seen in the diffraction pattern are lines which match Cr_2O_3, the original source of Cr, which indicates there is clearly an excess of Cr_2O_3 that was not doped into the lattice. Refined lattice parameters for the olivine phase are: $a = 10.326(1)$ Å, $b = 6.0050(9)$ Å, $c = 4.6934(8)$ Å, all of which represent $<0.1\%$ differences in the respective parameters from pristine $LiFePO_4$, and imply that the olivine lattice remains undoped by chromium.

Although this synthetic method does not indicate the presence of doping, the reduction of $LiFePO_4$ to Fe_2P at this lower temperature with hydrogen (as opposed to 850 °C *via* CTR) allows the formation of small quantities of a conductive additive

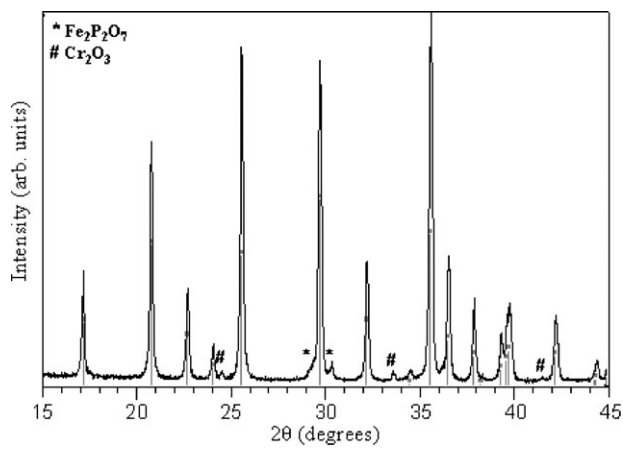

Fig. 11 A Cr-doped triphylite composition, $Li_{0.91}Cr_{0.03}FePO_4$, after firing at 600 °C for 15 h under Ar. The diffractogram shows the presence of Cr_2O_3 not incorporated into the olivine lattice and $Fe_2P_2O_7$, present in all lithium-deficient samples.

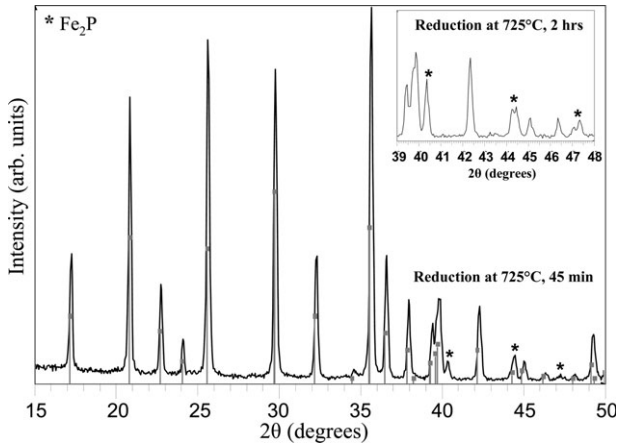

Fig. 12 XRD pattern of $LiFePO_4$ (from iron–oxalate precursors) subjected to further treatment at 725 °C in 7% H_2–N_2 for 45 min, causing a minor degree of reduction to Fe_2P. Iron phosphide is very evident after treatment for 2 h (inset).

without excessive growth in particle size. Samples of carbon-containing $LiFePO_4$ powder sintered at 600 °C were subjected to heat treatment at 725 °C under a 7% H_2–N_2 mixture for various lengths of time. Fig. 12 shows X-ray diffractograms after 45 min and 2 h. The presence of Fe_2P (inset) is clearly implicated after these relatively short heating times; Li_3PO_4 is also produced according to the reactions:

$$6LiFePO_4 + 13.5H_2 \rightarrow 3Fe_2P + 2Li_3PO_4 + H_3PO_4\uparrow + 12H_2O\uparrow$$

or

$$6LiFePO_4 + 16H_2 \rightarrow 2Fe_2P + 2Li_3PO_4 + 2FeP + 16H_2O\uparrow$$

and/or (in the presence of carbon from the precursor)

$$6LiFePO_4 + 8C \rightarrow 3Fe_2P + 2Li_3PO_4 + P\uparrow + 8CO_2\uparrow$$

We note that FeP is difficult to detect in the diffraction pattern, although it is visible by Mössbauer spectroscopy and Rietveld analysis of other materials produced by sol-gel methods, starting from iron(III) citrate.[36] The mechanism of hydrogen reduction of $LiFePO_4$ should be similar to that of carbon reduction; the $LiFePO_4$ surface groups which contact the hydrogen gas are most susceptible.

This is illustrated by a scanning electron microscopy image (Fig. 13) of a sample that has been reduced for only 45 min. Rutherford backscattering images taken from the SEM indicate the presence of phases which have different average atomic number (AAN); compounds of higher AAN will appear in brighter contrast in this mode. As a result, we can deduce that the large grey blocks in the micrograph are $LiFePO_4$ whose surface is speckled with tiny embedded crystals of Fe_2P (bright spots). As a result, the electrochemistry (Fig. 14) is vastly improved over $LiFePO_4$ powders sintered at 600 °C; the polarization is <0.2 V and the reversible capacity is 135 mA h g^{-1} at C/5. This brief reduction step allows the formation of a conductive surface layer of Fe_2P at a temperature low enough not to consume carbon or trigger large particle agglomeration, which in turn substantially improves the electrochemistry of $LiFePO_4$ prepared by a solid state route. Conversely, reduction for greater than one hour under 7% hydrogen at 725 °C has an adverse effect on battery performance; the material had poor reversibility (only 30% of theoretical capacity reached). This is likely to be a result of the phosphide covering the $LiFePO_4$ grain

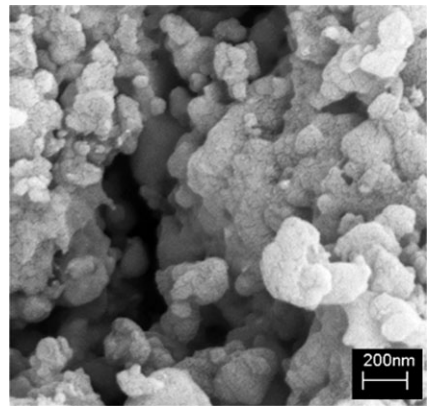

Fig. 13 SEM micrograph portraying Fe_2P (black dots) on the surface of $LiFePO_4$ after sintering the material at 725 °C in 7% H_2–N_2 for 45 min.

surface enough to limit Li transport in and out of the bulk grains, effectively smothering the $LiFePO_4$ crystallites.

The synthesis of $LiFePO_4$ under flowing ammonia produces conductive surface species at even lower temperatures (600 °C). This reaction produces both Fe_2P and metallic Fe_2N, detectable by XRD after only two hours of reaction time (Fig. 15), with Li_3PO_4 as a by-product. The formation of the nitride after shorter periods of time is apparent in SEM images that nicely illustrate 30–50 nm Fe_2N nanocrystallites littering the surface of the $LiFePO_4$ (Fig. 16). Selective EDX analysis of these regions (not quantitative) revealed atomic N : Fe ratios of 1 : 1. This is in contrast to $LiFePO_4$ treated in flowing Ar that showed no visual evidence for Fe_2N nanodots (inset Fig. 6, right) or any surface nitrogen species by EDX. XPS studies also confirm the presence of Fe_2N in the NH_3-treated materials, as shown by the N1s spectrum (insert, Fig. 16). The N1s core peak at 397.4 eV is in close accord with that reported for Fe_2N (399 eV). We note that the mechanism for the formation of these species is complex, since $LiFePO_4$ begins to crystallize at close to the same temperature that iron oxalate is nitrided to produce Fe_2N. As the temperature increases, the Fe_2N may react with $NH_4H_2PO_4$ to produce Fe_2P or Li_3PO_4 to produce $LiFePO_4$, or it may remain intact. Examination of the XRD pattern shows triphylite peaks that are broader compared with samples fired under argon or hydrogen at similar temperatures, indicating that the sample is poorly crystalline. As a result, electrochemical results for this compound have yet to be optimized.

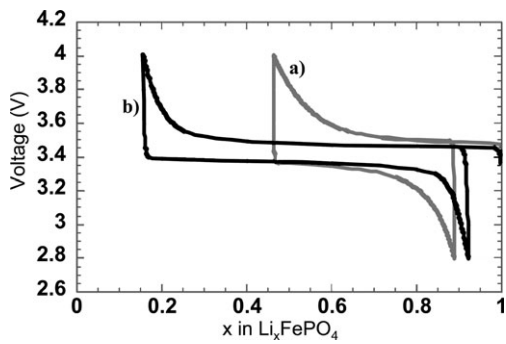

Fig. 14 Electrochemistry of (a) polycrystalline $LiFePO_4$ (600 °C, 15 h, Ar) and (b) the reduced triphylite composite (725 °C, 45 min, 7% H_2–N_2).

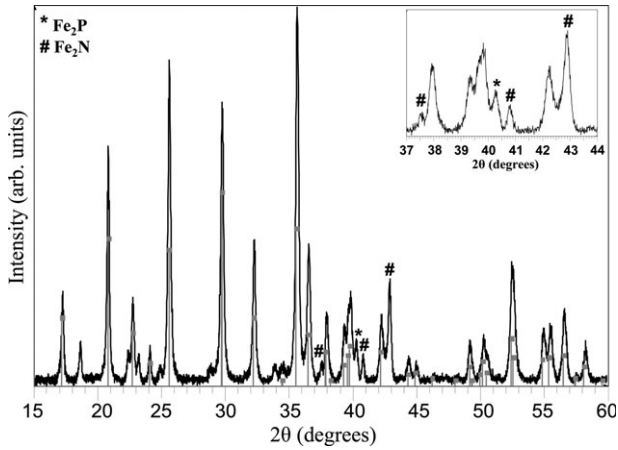

Fig. 15 X-Ray diffractogram of iron oxalate $LiFePO_4$ precursors, sintered under NH_3 (600°, 2 h). Both iron nitride (Fe_2N) and iron phosphide (Fe_2P) are present (inset).

(e) Small polaron hopping: correlation of electron mobility with lithium ion disorder

It is well known that extraction of lithium from $LiFePO_4$ results in formation of a two phase $LiFePO_4$–$FePO_4$ mixture owing, in part, to the 6% volume change between the phases. However, it was recently demonstrated that such two phase mixtures undergo a transition to a Li_xFePO_4 ($0 < x < 1$) solid solution at about 200 °C, where lithium ions and lithium vacancies randomly occupy the M1 sites within the lattice.[25] The presence of a mixed $Fe^{2+/3+}$ state on the M2 sites is implied, although only indirect evidence for it was derived from bond-sum data. This raises questions about the electron hopping rate between iron sites, and whether the electron delocalization which gives rise to this averaged valence state is coincident with lithium disordering. The latter phenomena are of importance, since electron transport in poor semiconductors such as $LiFePO_4$ takes place by small polaron migration, generated by either hole or electron carriers.[37] We chose to use variable temperature Mössbauer spectroscopy to probe the changes that occur as the material undergoes the phase transition. This technique can readily distinguish between Fe^{3+} and Fe^{2+} sites based on the difference between both isomer shift and quadrupole

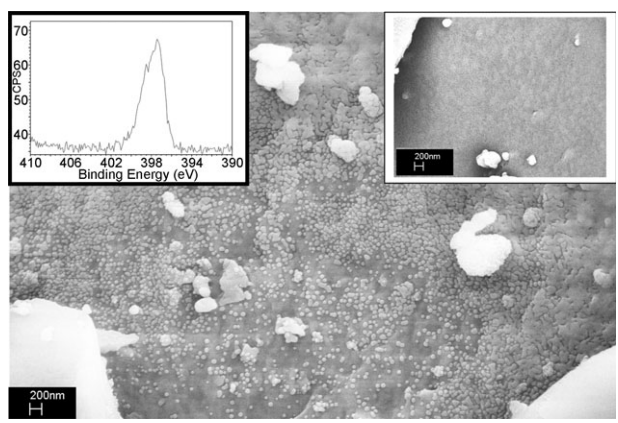

Fig. 16 SEM micrograph of $LiFePO_4$ treated at 600 °C under NH_3, showing surface Fe_2P and Fe_2N as nanodots. Inset left: XPS N1s spectrum; inset right, SEM micrograph at the same magnification of the same material treated under Ar at 600 °C instead of NH_3.

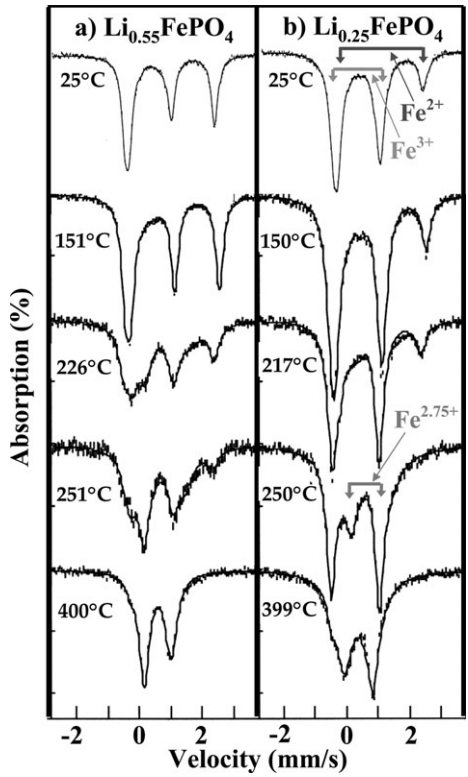

Fig. 17 Mössbauer spectra of chemically oxidized stoichiometries at room temperature and elevated temperatures illustrating the phase separation of the Fe^{2+}/Fe^{3+} components and the onset of solid solution behaviour, for (a) $Li_{0.55}FePO_4$ and (b) $Li_{0.25}FePO_4$.

splitting; moreover, it is sensitive to dynamics on timescales comparable to the Larmor precession time of the ^{57}Fe nucleus (about 10^{-8} s to about 10^{-6} s).[38] Rapid small polaron hopping between the Fe^{2+} and Fe^{3+} ions (*i.e.* $\ll 10^{-8}$ s) will show an averaged iron valence state, whereas a static situation or very slow hopping ($\gg 10^{-6}$ s) will distinguish between them. Thus, the onset of electron delocalization can be pinpointed and correlated to the lithium disordering temperature.

Samples of $LiFePO_4$ were oxidized using $NOBF_4$ to give two phase mixtures with nominal stoichiometries of $Li_{0.55}FePO_4$, $Li_{0.25}FePO_4$, and $FePO_4$. Mössbauer spectra recorded at room temperature of these two phase mixtures (Fig. 17a) contained contributions of the localised Fe^{2+} and Fe^{3+} components characterized by two doublets. They were fit with Mössbauer parameters of IS = 1.2 mm s^{-1}, QS = 3.0 mm s^{-1} and IS = 0.45 mm s^{-1}, QS = 1.5 mm s^{-1}, typical of Fe^{2+} and Fe^{3+} in these materials.[2] The relative two areas of the two components were in accord with the target starting stoichiometries. Mössbauer spectra recorded at temperatures from 130 to 430 °C illustrate the evolution from the initial two-phase composition to the solid solutions $Li_xFe^{2+/3+}PO_4$ as a function of temperature (Fig. 17b and c). The spectra of the samples at 150 °C still show the major features of the parent phases. Increases in temperature leads to the appearance of a new phase that grows in intensity as the parent phases diminish. Transformation to the single phase regime is essentially complete by 400 °C as shown by the collapse of the spectra to one doublet. The temperature dependence of the fitted parameters give the best illustration of the spectral changes as a function of heat treatment. The variation in the isomer shift of the Fe^{2+}/Fe^{3+} components and the solid solution phases in the

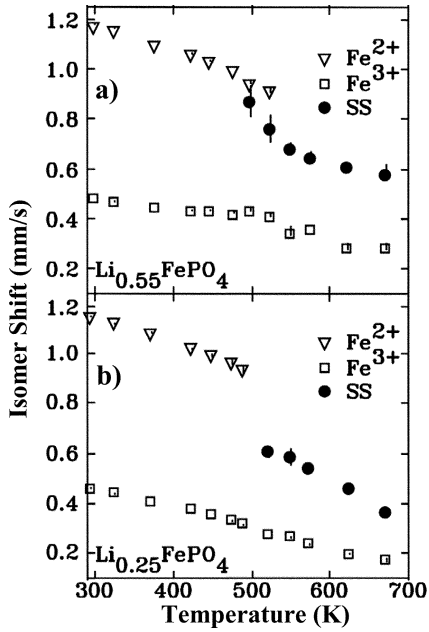

Fig. 18 Iron isomer shifts measured by Mössbauer spectroscopy for the Fe^{2+}, Fe^{3+} and solid solution phases of (a) $Li_{0.55}FePO_4$ and (b) $Li_{0.25}FePO_4$ at various temperatures.

phases $Li_{0.55}FePO_4$ (Fig. 18a) and $Li_{0.25}FePO_4$ (Fig. 18b) clearly show that the isomer shift of the solid solution phase lies between those of the parent Fe^{2+} and Fe^{3+} phases in both cases. Thus the $Li_{0.55}FePO_4$ phase displays a single quadrupole doublet with an isomer shift of 0.9 mm s^{-1} at 250 °C, midway between that of the parent phases. This demonstrates that the iron valence is intermediate between 2+ and 3+ in this rapid hopping regime, where the valence states are averaged on the timescale of the Mössbauer window. We can identify the exact temperature of the phase transition by the appearance of the averaged signal.

Both samples show an onset of rapid electron hopping behavior at about 225 °C, which is the same temperature as the onset of the transformation of two-phase mixtures of $LiFePO_4$–$FePO_4$ into a solid solution reported in the literature.[25,39] These two XRD studies demonstrated that the patterns for the two parent phases merge into one single phase Li_xFePO_4 that displays intermediate lattice parameters. The temperature at which this occurs is relatively invariant as a function of composition "x". Subsequent neutron diffraction studies have also revealed that the lithium ions are fully disordered in the solid solutions.[40] Our Mössbauer studies take us one step further in understanding the formation of the solid solution. Namely, the spectrum would not change during the phase transition if the delocalization of the lithium within the lattice led to a static delocalized distribution of the Fe^{2+} and Fe^{3+}. The clear evolution of the spectra within the Mössbauer "window" in which changes are evident shows that the electrons are dynamically delocalized in this rapid small polaron hopping regime. It is this behavior that is correlated with the random lithium population within the solid solution.

We believe that the averaging of the iron oxidation state induces disorder of the Li^+, rather than the converse. This supposition is based on comparison to our previous work on complex phase transitions driven by lithium de/intercalation in $Li_{3-x}V_2(PO_4)_3$, where a combination of charge ordering on the vanadium sites and lithium ordering/disordering amongst lattice sites was shown to be responsible for the features in the electrochemical curve.[24,41] Combined neutron diffraction, ^7Li

NMR and electrochemical studies revealed that two-phase transition behavior between single phase compositions corresponding to $x = 0$, 0.5, 1.0, 2.0 and 3.0 was adopted on lithium extraction. The single phases are characterized by highly localized V^{3+}/V^{4+} valence populations, and specific Li sites. However, solid solution electrochemical behavior was observed on insertion of Li^+ (and e^-), and was correlated with the delocalization of both lithium and the V^{n+} valence states as seen by diffraction and NMR. The driving force here was proposed to arise from disorder of the mixed V^{4+}/V^{5+} state in $V_2(PO_4)_3$ formed on emptying the lattice that then gave rise to random lithium siting on re-insertion. That is, lithium insertion results in disorder (in the absence of V^{n+} ordering to drive Li^+ ordering). The results suggested that Li-site ordering and the electron ordering are coupled. It also explains why valence substitution can drive the formation of solid solution regimes. For example, the solid solution γ-phase of $Li_3V_2(PO_4)_3$ that is only accessible above 450 K, is stabilized at room temperature by the addition of a M^{4+} dopant such as Zr^{4+} to form $Li_{3-x}(V_{1-x}Zr_x)_2(PO_4)_3$.

Conclusions

The tailoring of carrier transport in poorly conductive lithium metal phosphates hinges on the ability to precisely control bulk crystal chemistry, particle morphology, and surface chemistry, and the understanding of cooperative ion/electron transport in these highly localized systems. Our studies of the olivine phosphates show that aliovalent dopants do not contribute to the high conductivity observed in olivine phosphates treated at high temperatures under carbothermal or reducing conditions. There is also no evidence for significant dopant concentration in the olivine lattice—nor its stabilization of stable, substoichiometric lithium phases on treatment at processing temperatures that lead to high conductivity. The latter can be obtained in composite materials, however, through exploiting the reactivity of the phosphate surface. Partial reduction, either through carbothermal reduction and/or treatment in H_2 or treatment in ammonia forms metallic surface species (phosphides or nitrides respectively). Along with the residual carbon, these nanophase composites are highly conductive. This explains the properties of Cr-doped $LiFePO_4$. Ellingham curves can be used to determine the temperature at which carbothermal reduction occurs, to give an estimate of the reducibility of the phosphate. Therefore, although Fe, Co and Ni olivines are highly susceptible to reduction, Mn is not, and such species cannot be readily formed at temperatures $< 1000\ ^\circ C$. Establishing control of the concentration, growth and placement of such metallic species is crucial to nanostructure optimization. Understanding the interface, and how electrons are delivered to the bulk, is also of vital importance. New surface modification methods can be anticipated in the future, which will provide even better nanophase conductivity in insulating or poorly conductive materials.

With respect to bulk transport properties, all lithium metal phosphates studied to date undergo two-phase transformations upon extraction of lithium from the lattice. The movement of the phase boundary represents a migration of both carriers: the electrons or holes (*i.e.* small polarons) and the lithium ions. The formation of solid solutions at elevated temperature can in principle enhance the mobility. In this regime in Li_xFePO_4, the rapid hopping of the small polarons can be probed by Mössbauer spectroscopy, which provides an accurate measure of when the $Fe^{2+/3+}$ sites become averaged on the Mössbauer time scale, and also provides an estimate of the hop frequency. The onset of lithium ion disorder is precisely correlated with the onset of rapid small polaron hopping, indicating that the two transport mechanisms are coupled. The transport is limited by neither carrier alone, but by their concerted mobility through the lattice, *i.e.*, the migration of the phase boundary. This is expected to be a general phenomenon for lithium metal phosphates. Consideration of these factors may lead to methods by which solid solutions can be induced to form at room temperature through manipulation of the lattice energetics.

Acknowledgements

We gratefully acknowledge funding from NSERC (Canada) through its Discovery Grant Program. LFN especially thanks NSERC for support from the Canada Research Chair program.

References

1 (*a*) A. K. Padhi, K. S. Nanjundaswamy and J. B. Goodenough, *J. Electrochem. Soc*., 1997, **144**, 1188–1194; (*b*) J. B. Goodenough, A. K. Padhi, C. Masquelier and K. S. Nanjundaswamy, US Patent 08/840,523, 1997.
2 G. Li, H. Azuma and M. Tohda, *Electrochem. Solid-State Lett*., 2002, **5**, A135.
3 (*a*) H. Huang, S.-C. Yin, T. Kerr and L. F. Nazar, *Adv. Mater*., 2002, **14**, 1525; (*b*) J. Barker and M. Y. Saidi, US Patent, 5,871,866, 1999; (*c*) M. Y. Saïdi, J. Barker, H. Huang and G. Adamson, *Electrochem. Solid-State Lett*., 2002, **5**, A149; (*d*) S. C. Yin, P. Strobel, M. Anne and L. F. Nazar, *J. Am. Chem. Soc*., 2003, **125**, 10402.
4 (*a*) J. Barker, M. Y. Saidi and J. L. Swoyer, *J. Electrochem. Soc*., 2003, **150**, A1394; (*b*) J. Barker, M. Y. Saidi and J. Swoyer, US Patent 6,387,568, 2002; (*c*) J. Barker, M. Y. Saidi and J. L. Swoyer, *Electrochem. Solid-State Lett*., 2003, **6**, A1.
5 A. Yamada, S. C. Chung and K. Hinokuma, *J. Electrochem. Soc*., 2001, **148**, A224.
6 (*a*) K. S. Nanjundaswamy, A. K. Padhi, J. B. Goodenough, S. Okada, H. Ohtsuka, H. Arai and J. Yamaki, *Solid State Ionics*, 1996, **92**, 1; (*b*) A. K. Padhi, K. S. V. Manivannan and J. B. Goodenough, *J. Electrochem. Soc*., 1998, **145**, 1518; (*c*) C. Masquelier, A. K. Padhi, K. S. Nanjundaswamy and J. B. Goodenough, *J. Solid State Chem*., 1998, **135**, 228.
7 A. Yamada and S.-C. Chung, *J. Electrochem. Soc*., 2001, **148**, A960.
8 M. Yonemura, A. Yamada, Y. Takei, N. Sonoyama and R. Kanno, *J. Electrochem. Soc*., 2004, **151**, A1352.
9 C. Delacourt, P. Poizot, M. Morcrette, J.-M. Tarascon and C. Masquelier, *Chem. Mater*., 2004, **16**, 93.
10 K. Amine, H. Yasuda and M. Yamachi, *Electrochem. Solid-State Lett*., 2000, **3**, 178.
11 D. Morgan, A. Van der Ven and G. Ceder, *Electrochem. Solid-State Lett*., 2004, **7**, A30.
12 M. S. Whittingham, Y. Song, S. Lutta, P. Y. Zavalij and N. A. Chernova, *J. Mater. Chem*., 2005, **15**, 3362.
13 F. Zhou, K. Kang, T. Maxisch, G. Ceder and D. Morgan, *Solid State Commun*., 2004, **132**, 181.
14 T. Maxisch, F. Zhou and G. Ceder, *Phys. Rev. B*, 2006, **73**, 104301.
15 (*a*) N. Ravet, Y. Chouinard, J. F. Magnan, S. Besner, M. Gauthier and M. Armand, *J. Power Sources*, 2001, **97**, 503; (*b*) N. Ravet and M. Armand, US Patent Application 0195591A1, 2002.
16 H. Huang, S. C. Yin and L. F. Nazar, *Electrochem. Solid-State Lett*., 2001, **4**, A170.
17 F. Croce, A. D'Epifanio, J. Hassoun, A. Deptula, T. Olczac and B. Scrosati, *Electrochem. Solid-State Lett*., 2002, **5**, A47.
18 S.-Y. Chung, J. T. Bloking and Y.-M. Chiang, *Nat. Mater*., 2002, **123**, 1.
19 J. Barker, M. Y. Saidi and J. L. Swoyer, *Electrochem. Solid-State Lett*., 2003, **6**, A53.
20 S.-Y. Chung and Y.-M. Chiang, *Electrochem. Solid-State Lett*., 2003, **6**, A278.
21 B. Ellis, P. S. Herle and L. F. Nazar, Abstract #1074, *203rd Electrochemical Society Spring Meeting*, Paris, April, 2003.
22 P. S. Herle, B. Ellis and L. F. Nazar, *Nat. Mater*., 2004, **3**, 147.
23 S. Q. Shi, L. J. Liu, C. Ouyang, D. S. Wang, Z. X. Wang, L. Q. Chen and X. J. Huang, *Phys. Rev. B*, 2003, **68**, 195108.
24 S. C. Yin, H. Grondey, P. Strobel, M. Anne and L. F. Nazar, *J. Am. Chem. Soc*., 2003, **125**, 10402.
25 C. Delacourt, P. Poizot, J.-M. Tarascon and C. Masquelier, *Nat. Mater*., 2005, **4**, 254.
26 B. H. Toby, *EXPGUI*, a graphical user interface for *GSAS*, *J. Appl. Crystallogr*., 2001, **34**, 210–213.
27 S. Yang, Y. Song, P. Y. Zavalij and M. S. Whittingham, *Electrochem. Commun*., 2002, **4**, 239.
28 A. Goni, L. Lezama, M. I. Arriortura, G. E. Barberis and T. Rojo, *J. Mater. Chem*., 2000, **10**, 423.
29 C. Delacourt, C. Wurm, L. Laffont, J.-B. Leriche and C. Masquelier, *Solid State Ionics*, 2006, **177**, 333.
30 M. Saiful Islam, D. J. Driscoll, C. A. J. Fisher and P. R. Slater, *Chem. Mater*., 2005, **17**, 5085.

31 A. Yamada, H. Koizumi, S.-I. Nishimura, N. Sonoyama, R. Kanno, M. Yonemura, T. Nakamura and Y. Kobayashi, *Nat. Mater.*, 2006, **5**, 357.
32 R. Brochu, A. Lamzibri, A. Aadane, S. Arsalane and M. Ziyad, *Eur. J. Solid State Inorg. Chem.*, 1991, **28**, 253.
33 J. W. Evans and L. C. DeJonghe, *The Production of Inorganic Materials*, Macmillan, New York, 1991, p. 64.
34 M. Doeff, Y. Hu, F. McLarnon and R. Kostecki, *Electrochem. Solid-State Lett.*, 2003, **6**, A207.
35 (*a*) M. Armand, M. Gauthier, J.-F. Magnan and N. Ravet, 2002, PCT WO 02/27824; (*b*) R. Dominko, J. M. Goupil, M. Bele, M. Gaberscek, M. Remskar, D. Hanzel and J. Jamnik, *J. Electrochem. Soc.*, 2005, **152**, A858.
36 Y.-H. Rho, L. F. Nazar, L. Perry and D. Ryan, *J. Electrochem. Soc.*, in press.
37 K. M. Rosso, D. M. A. Smith and M. Dupuis, *J. Chem. Phys.*, 2003, **118**, 6455.
38 S. Dattagupta, in *Mössbauer Spectroscopy*, ed. D. P. E. Dickson and F. J. Berry, Cambridge University Press, Cambridge, 1986, p. 198.
39 J. L. Dodd, R. Yazami and B. Fultz, *Electrochem. Solid-State Lett.*, 2006, **9**, 131.
40 C. Delacourt, J. Rodríguez-Carvajal, B. Schmitt, J.-M. Tarascon and C. Masquelier, *Solid State Sci.*, 2005, **7**, 1506.
41 S.-C. Yin, H. Grondey, P. Strobel and L. F. Nazar, *J. Am. Chem. Soc.*, 2003, **125**, 327.